Actinic detection of sub-100 nm defects on extreme ultraviolet lithography mask blanks

Seongtae Jeong,[a] Lewis Johnson, and Seno Rekawa
Center for X-Ray Optics, Lawrence Berkeley National Laboratory, Berkeley, California 94720

Chris C. Walton and Shon T. Prisbrey
Lawrence Livermore National Laboratory, Livermore, California 94550

Edita Tejnil
Intel Corporation, Santa Clara, California 95052

James H. Underwood
Center for X-Ray Optics, Lawrence Berkeley National Laboratory, Berkeley, California 94720

Jeffrey Bokor
Center for X-Ray Optics, Lawrence Berkeley National Laboratory, Berkeley, California 94720 and EECS Department, University of California, Berkeley, California 94720

(Received 2 June 1999; accepted 2 September 1999)

We present recent experimental results from a prototype actinic (operates at the 13 nm extreme ultraviolet wavelength) defect inspection system for extreme ultraviolet lithography mask blanks. The defect sensitivity of the current actinic inspection system is shown to reach 100 nm in experiments with programmed defects. A method to cross register and cross correlate between the actinic inspection system and a commercial visible-light scattering defect inspection system is also demonstrated. Thus, random, native defects identified using the visible-light tool can reliably be found and scanned by our actinic tool. We found that native defects as small as 86 nm (as classified by the visible-light tool) were detectable by the actinic tool. These results demonstrate the capability of this tool for independent defect counting experiments. © *1999 American Vacuum Society.* [S0734-211X(99)10906-5]

I. INTRODUCTION

Extreme ultraviolet lithography (EUVL) is one of the leading candidates for fabrication of integrated circuits with critical dimensions less than 100 nm.[1] Utilizing 11–14 nm radiation and all-reflective optical elements based on Mo/Si or Mo/Be multilayer coatings, EUVL is expected to cover several device generations down to 30 nm. The mask architecture pursued for EUVL is a reflective one. A multilayer reflection coating constructed on a robust substrate such as a Si wafer or glass plate forms the EUVL mask blank and the circuit pattern is defined with patterned absorber on top of the blank.

Defects in the EUVL mask pose a serious concern as in other advanced lithography technologies. In EUVL masks, critical defects can arise either from flaws in the absorber pattern or from defects in the multilayer coating. While techniques for repairing defects in the absorber pattern have been demonstrated,[2] repair of defects in the multilayer coating is problematic. Defects in or below the multilayer can either disrupt the multilayer, reducing the reflectivity (opaque defect or amplitude defect), or can generate a conformal multilayer topography inducing a phase error in the reflected electric field (phase defect). These opaque or phase defects on the mask blank can have a significant effect on the final aerial image.[3,4] For the 100 nm device generation, the lateral dimension of critical defects on the mask is estimated to be comparable to or even smaller than 80 nm[4] and the density of these critical defects must be reduced to the level approaching 0.01 defects per cm^2. Therefore, establishment of the capabilities to produce EUVL mask blanks with a sufficiently low defect density is a major challenge. Meeting this challenge is crucial for the success of EUVL technology.

Inspection of produced mask blanks for any critical defect is an integral step in demonstrating a low defect density EUVL mask blank. Because the proposed form factor of the EUVL mask blank is similar to that of the standard silicon wafer, research on the application of conventional wafer inspection technologies such as atomic force microscopy (AFM) and scanning electron microscopy (SEM) for inspecting EUVL mask blanks is being actively pursued. In particular, optical scattering wafer inspection tools, which measure the optical scattering cross section of defects, have been most heavily used for inspection of EUVL mask blanks due to their high throughput, high sensitivity, and commercial availability. However, these tools tend to have a limited probing depth into the multilayer and it is uncertain whether current optical inspection tools can capture all the EUV printable defects. Therefore, at least at the initial developmental stage of multilayer deposition and inspection technology, an actinic (at-wavelength) inspection is highly desirable to capture all the defects on an EUVL mask blank. Actinic inspection directly probes the effect of a defect on the reflected electric field and helps to assess the printability of the defect. An actinic inspection system also helps to establish a nonactinic

[a]Electronic mail: stjeong@lbl.gov

inspection strategy for ultimate commercial use via cross correlation of the EUV response of defects with their optical response.

In a previous publications,[5] we reported on a proof-of-concept inspection system, referred to as an EUV scanner, based on raster scanning the EUVL mask blank under a focused EUV beam. Briefly, when a focused EUV beam is incident on a defect, the defect will induce a decrease in the intensity of the specularly reflected beam (bright field detection) and scattering of photons into nonspecular directions (dark field detection). The detector assembly is constructed for simultaneous bright field and dark field detection. For dark field detection, a microchannel plate detector is used with a hole at the center to pass the speculary reflected beam which is captured by the bright field detector situated behind the microchannel plate. The small focal spot on the sample is formed by imaging an EUV-illuminated aperture using a pair of curved, glancing angle mirrors in a Kirkpatrick–Baez configuration. The focal spot size can be varied simply by using object apertures of different sizes. The smallest spot size we have produced so far is 2.5 μm by 4μm when a 30 μm by 10 μm aperture is used. The spot size is currently limited by aberrations and efforts to reduce the aberration and improve the spot size are currently underway. The EUV scanner system is installed at Beamline 11.3.2 of Advanced Light Source at Lawrence Berkeley National Laboratory.

Through experiments with programmed defect samples, it has been demonstrated that the current EUV scanner can detect both amplitude and phase defects with varying topography and submicron lateral dimensions.[6] In this article, we report on more recent results showing that the current system can detect defects below 100 nm in lateral dimension. We also report on successful demonstration of cross registration of the current EUV scanner with an optical scattering inspection tool and an atomic force microscope so that randomly occurring, native defects found in one tool can be studied with each of the others. In the initial cross-correlation experiment, a defect as small as 86 nm was successfully detected with the EUV scanner.

II. SENSITIVITY OF THE ACTINIC INSPECTION SYSTEM

Considering the fact that the dimensions of critical defects on a 4X reduction EUVL mask are smaller than 100 nm (for the 100 nm device generation), the inspection system must be capable of detecting defects in the 100 nm range. In order to evaluate the sensitivity of an inspection system, calibration of the detected signal for a defect of known size is highly desired. For the purposes of this calibration, programmed opaque defects with well-defined geometry are preferable to phase defects whose properties are more complicated. Therefore, a specially prepared, programmed opaque defect sample was employed to calibrate the sensitivity of the current EUV scanner. Because the achievable size of the isolated defects was limited by the capability of the optical lithography that was used to fabricate them, we used a partially opaque defect to simulate a smaller, but totally opaque defect. The defects were fabricated by depositing and patterning a thin layer of silicon dioxide on top of a multilayer coated silicon wafer. The layout of the programmed defects are 5×5 array of isolated rectangles at 80 μm intervals as described in Ref. 5. Relatively larger rectangles were also made for the purpose of characterizing the silicon dioxide film. The thickness of the oxide was independently measured to be 11 nm and the amount of absorption due to the oxide layer was measured in the EUV scanner to be 20% relative to the clear region. The size of the defects were measured independently using SEM and the lateral size of the smallest defect was found to be 300 nm. Figure 1(a) shows a bright field line scan along the row containing the earlier-mentioned 300 nm, 20% opaque defect, in addition to larger defects. Indeed this defect generates the small dip in the bright field signal with observed magnitude of 0.12%. Because the signal level generated from a defect being sought approaches 0.1%, care must be taken to align the bright field detector so that the effect of beam steering due to midspatial frequency roughness of the mask blank can be suppressed well below 0.1% level.[6] This effect causes a reproducible background fluctuation that does not average out. The random background noise level is suppressed below 0.08% level by averaging ten identical scans. The major source of random noise at the present moment is due to vibration of the optical elements in the beamline. The current system images a pinhole that is somewhat overfilled by the beamline optics. Any relative movement between the spot that illuminates the pinhole and the pinhole itself induces a variation in the total energy transmitted through the pinhole. This variation will appear in both the bright field and dark field signals.

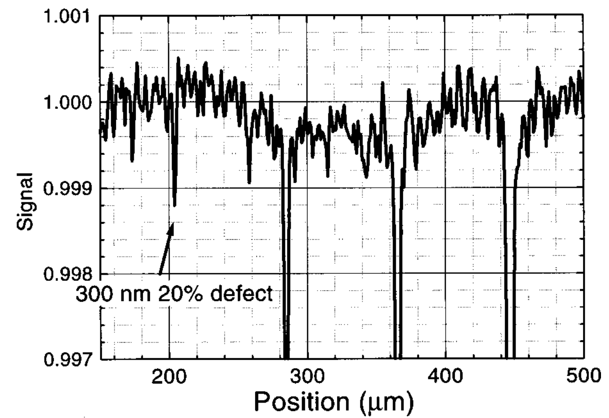

FIG. 1. Averaged line scan along the row containing the 300 nm 20% opaque defect. The bright field signal reveals a dip of 0.12% due to the defect. The noise in the bright field detection is dominated by the vibration of the beamline optics.

In terms of attenuation of the reflected EUV radiation by absorption, a 20% opaque defect with dimensions of 300 nm by 300 nm is equivalent to a totally opaque defect with dimensions of 130 nm by 130 nm. Although the contribution to the bright field reduction from a defect can come from scattering out of the solid angle subtended by the bright field detector as well as the absorption, the effect of scattering will

increase the reduction of the bright field signal. Therefore, the estimate of the bright field signal reduction based on *absorption only* can be considered as conservative. The fact that the current system is capable of detecting 300 nm wide 20% opaque defects indicates that the sensitivity of the current inspection system approaches 100 nm for totally opaque defects. Further reduction in probe spot size will increase the sensitivity. While the bright field shows a dip for partially opaque programmed defects, the dark field scan (not shown) shows virtually no sensitivity to partially opaque defects. This is consistent with the previously reported observation that opaque programmed defects show much less visibility in the dark field than phase programmed defects, which show relatively high visibility in the dark field.[6]

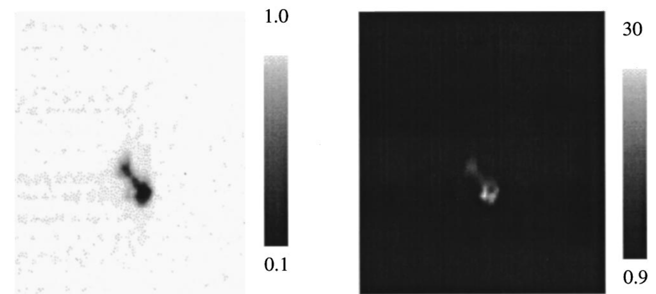

FIG. 2. Displayed are at-wavelength bright field (left) and dark field (right) scan over a diamond scribe mark. The spatial scale of the picture is 200 μm on the side for both pictures. Note the scale in the dark field. The diamond scribe mark scatters 29 times higher than the background scattering. A structure inside the scribe mark is visible in the dark field image.

III. CROSS CORRELATION WITH AN OPTICAL SCATTERING INSPECTION SYSTEM

Although the programmed defect with its well-defined geometry provides a way of calibrating the inspection system, actual native defects found in the mask blanks generally have irregular shapes.[7] This influences the optical scattering cross section as well as the EUV response. Studying the morphology and composition of defects is very important for revealing the source of the defects and possibly controlling them. Once a defect is found using an optical scattering inspection tool that provides the optical cross section of the defect along with its coordinates, its morphology and composition can be studied with AFM and SEM with compositional analysis capability. In Ref. 7, Burkhart *et al.* reported successful cross registration among an atomic force microscope, a scanning electron microscope, and a high throughput optical defect inspection tool (KLA Tencor SP1). In this section, we report a successful cross registration between the earlier-mentioned inspection tools and the EUV scanner. Cross registration of the EUV scanner with these nonactinic inspection tools and the capability to detect *the same* defect with a variety of tools provides important advantages. First, the effect of a real defect on the reflected EUV electric field and therefore its printability can be assessed with the help of the EUV scanner. Second, comparison between the response of the SP1 with the EUV response of defects of various sizes and types can reveal the degree of correlation between the optical scattering cross section of a defect and its EUV responses.

Because the current throughput of these systems differ by several orders of magnitude, the only realistic approach for cross registration between the EUV scanner and the SP1 is to employ fiducials at well-defined positions on the mask blank. Since the 150 mm mask blanks currently fabricated at Lawrence Livermore National Laboratory do not have any embedded fiducial marks, a diamond scribe was used to create large alignment marks near the center of the sample. Only a gentle contact of a sharp regular diamond scribe was found to be necessary to create a mark as large as 20 μm without generating much debris. These alignment marks can be easily detected in the SP1. As a result, a list of defects found by the SP1 is provided with their optical scattering cross sections and coordinates as well as the coordinates of the alignment marks. The alignment mark created with a diamond scribe shows very high EUV scattering as well as a significant reflectivity reduction. Figures 2(a) and 2(b) show the bright field and dark field actinic image of the diamond scribe alignment mark taken with EUV scanner. The peak dark field signal strength is 29 times the background dark field signal. The high scattering may come from the roughness of the multilayer created by the diamond scribe tip. Because the alignment mark is large and generates high scattering, a relatively large EUV beam with a large pixel size can be used to find the alignment mark relatively rapidly. Once at least two alignment marks are found, the cross registration between the two systems is complete.

For the initial experiments, a total of 23 defects on a Mo/Si multilayer found by the SP1 were scanned in the EUV scanner. The sample was made by depositing 81 alternating layers of Mo/Si in the ion beam sputtering deposition chamber at Lawrence Livermore National Laboratory. Most of the defects show very pronounced signals in the dark field. Figure 3 (a) shows the correlation between the bright field signal and dark field signal for 23 defects. The bright field signal is defined as the fractional *reduction* of the bright field detector output relative to the neighboring clear region. The dark field signal is defined as the fractional *increase* in the dark field detector output relative to the background level.[6] There is a relatively good correlation between the bright field signal and dark field signal for most of the defects except four. The straight line in Fig. 3(a) is the best-fit power law when the four points are excluded. The good correlation between the bright field and dark field suggests that the bright field reduction is primarily due to scattering. In contrast, when the bright field reduction is dominated by EUV absorption, as in the case of the partially opaque defects discussed in Sec. II; the corresponding points tend to lie in the region where the dark field signal is relatively lower compared to the bright field signal. In Fig. 3(a), the exponent of the power law is less than unity, which would be obtained if all of the photons scattered out of the bright field detector are detected by the dark field detector. In the current detector configuration, there is a dead region between two detectors, and the sublinear dependence can be qualitatively explained by the dependence of the scattering angle on the defect size. For example,

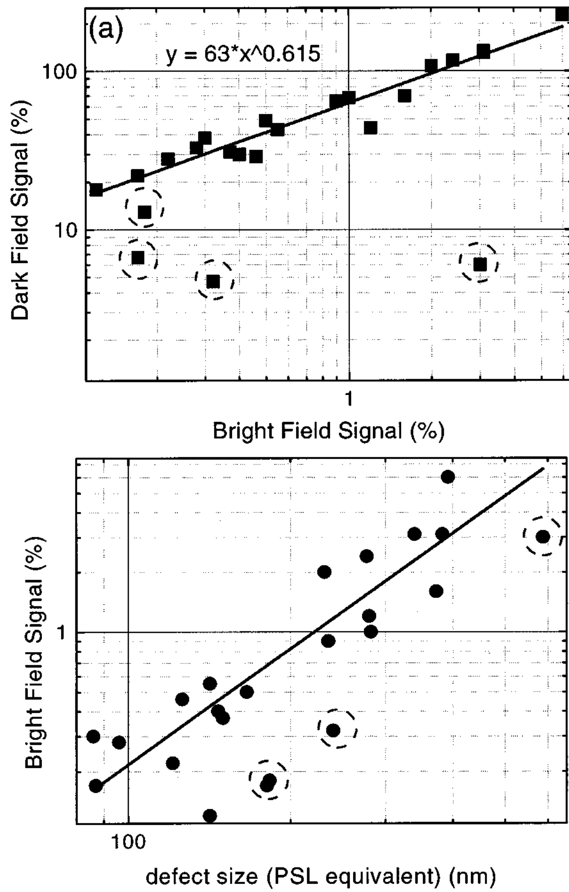

FIG. 3. (a) Correlation between the bright field signal and the dark field signal is displayed for 23 defects that are scanned. The line is the best fit power law when the four outlying points are excluded. Outliers are enclosed in dashed circles. (b) The PSL equivalent defect size vs at-wavelength bright field signal is displayed for 23 defects. Note that there is a general correlation between two inspection systems. The line is the best-fit power law when the five outlying points are excluded. The exponent is 1.93.

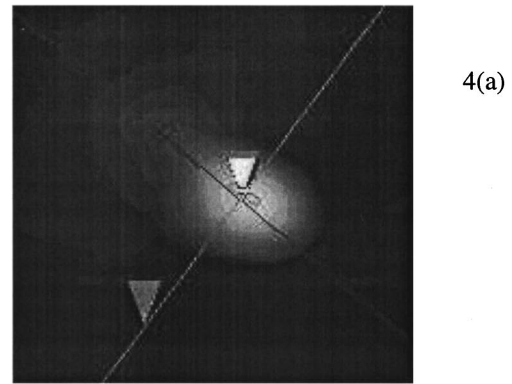

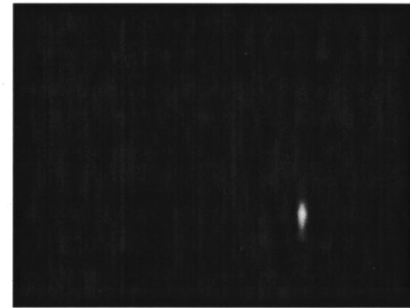

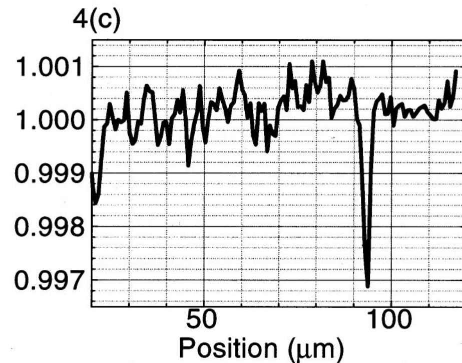

FIG. 4. (a) AFM picture of the 86 nm defect. The spacing between the arrowheads is 96 nm. The height of the defect is 44 nm. The horizontal scale of the picture is 220 nm. (b) Actinic dark field scan over the 86 nm defect is shown. The dark field signal from this defect is 38% while the background signal fluctuation is $\sigma = 0.8\%$. The dimension of the scan is 100 μm by 75 μm. (c) Bright field line scan along the row containing the defect is shown. The defect induced 0.3% change in the bright field.

for a large defect (which shows stronger bright field signal as will be shown later) the scattering angle is so small that some of the photons might not be captured by the dark field detector. One might suspect that the sublinear dependence between bright field and dark field signal strength might also come from the saturation of the dark field detector at higher signal levels. However, a careful experiment at various incoming beam intensities reveals that the dark field detector shows excellent linearity over the range plotted in Fig. 3(a).

Figure 3(b) displays the bright field signal versus the defect size reported by the SP1. The SP1 size represents the size of a polystyrene latex (PSL) sphere showing the same amount of scattering of the visible laser radiation as the defect. There is a *general* correlation between the actinic bright field signal and PSL equivalent size for all 23 defects except for five defects located rather low in the graph. The line in Fig. 3(b) is the best-fit power law when the five outlying points are excluded. The best-fit exponent for the remaining 18 points is 1.93, indicating that the EUV signal generally scales with the area of the defect.

Despite the general trend in Figs. 3(a) and 3(b), there is an appreciable spread in the data points. For example, the five points that are excluded in deriving the best-fit power law in Fig. 3(b) display deviation from the best-fit line. Interestingly, four out of these five defects (circled with dashes) are the same ones that did not lie close to the best-fit line in Fig. 3(a), either. The nature of such outlying defects will be an important subject for further investigation. Furthermore, even the defects included in the curve fitting display a significant degree of spread. For example, the defect with PSL equivalent size 121 nm [fourth point from the left in Fig. 3(b)] shows less bright field signal than one with 86 nm PSL equivalent size. It is well known that there can be a difference between the physical size and PSL equivalent size of a defect depending on its shape and composition.[8] This cer-

tainly contributes to the spread in the data. Clearly, further comparison with AFM and SEM data is warranted to obtain better understanding. In the future, more statistics as shown in Figs. 3(a) and 3(b) will be compiled for different kinds of defects. For example, defects on top of the multilayer coating might display different statistics compared to defects buried under the multilayer when plotted as in Figs. 3(a) and 3(b). If that is the case, the information can be used for simple defect classification.

In Fig. 3(b), three of the native defects exhibit PSL equivalent size less than 100 nm. The AFM scans taken over these three defects reveal that their lateral dimensions are indeed smaller than 100 nm (full width half maximum) with peak defect height in the neighborhood of 50 nm. An actinic dark field scan of one of those sub-100 nm defects along with its AFM scan are shown in Figs. 4(a) and 4(b), respectively. The bright field line scan along the row containing the defect is shown in Fig. 4(c). The line scan shown in Fig. 4(c) is an average of ten identical scans to suppress the noise due to the vibration of the beamline optics. The PSL equivalent size of this defect is 86 nm as given by the SP1. The signal strength of the defect is 38% in the dark field (not shown) and 0.3% in the bright field. The background root-mean-square dark field fluctuation due to roughness is measured to be $\sigma = 0.8\%$. Therefore, the 38% dark field signal corresponds to 47.5σ. The fluctuation in the bright field is $\sigma = 0.05\%$. This result confirms that the current EUV scanner can detect defects smaller than 100 nm in lateral size.

IV. CONCLUSION

We have conducted experiments to evaluate the sensitivity of the at-wavelength defect inspection system. It has the capability to detect defects in the 100 nm range, as confirmed in experiments with a programmed defect sample and in an experiment conducted in cross correlation with a visible defect inspection tool. We have also demonstrated the capability to cross register the current EUV scanner with other inspection and metrology tools in order to detect and characterize real defects on EUVL mask blanks. From an initial experiment, it is noted that there exists a general correlation between the PSL equivalent defect size measured by the optical inspection tool and signals in the EUV inspection system. More experiments are planned to compile statistics on EUV characteristics of real defects.

ACKNOWLEDGMENTS

This work is supported by the Extreme Ultraviolet Lithography Limited Liability Company (EUV LLC), the Office of Energy Research, Basic Energy Sciences, of the U.S. Department of Energy under Contract No. DE-AC03-76SF00098, SRC Contract No. 96-LC-460 and DARPA Grant No. MDA972-97-1-0010.

[1]See Proc. SPIE **3331**, 2 (1998).
[2]P. Yan, S. Yan, G. Zhang, J. Richards, P. Kofron, and J. Chow, 18th Annual Symposium on Photomask Technology and Management, Redwood City, California, 16–18 September 1998 [Proc. SPIE **3546**, 206 (1998)].
[3]K. Nguyen, Ph.D. dissertation, University of California, Berkeley, 1994.
[4]Y. Lin and J. Bokor, J. Vac. Sci. Technol. B **15**, 2467 (1997).
[5]S. Jeong *et al.*, J. Vac. Sci. Technol. B **16**, 3430 (1998).
[6]S. Jeong *et al.*, Proc. SPIE **3676**, 298 (1999).
[7]S. Burkhart, C. Cerjan, S. Vernon, and C. Walton, Proc. SPIE **3676**, 570 (1999).
[8]Abbie Warrick, Lawrence Livermore National Laboratory (private communication).